ACSNANO www.acsnano.org

ARTICLE

Oxygen Nanobubble Tracking by Light Scattering in Single Cells and Tissues

Pushpak Bhandari,[†,§] Xiaolei Wang,[‡,§] and Joseph Irudayaraj*[,†]

[†]Department of Agricultural and Biological Engineering, Bindley Bioscience Center, Purdue Center for Cancer Research, Purdue University, West Lafayette, Indiana 47907, United States

[‡]University of Chicago, James Franck Institute, 929 E 57th Street, Chicago, Illinois 60637, United States

Supporting Information

ABSTRACT: Oxygen nanobubbles (ONBs) have significant potential in targeted imaging and treatment in cancer diagnosis and therapy. Precise localization and tracking of single ONBs is demonstrated based on hyperspectral dark-field microscope (HSDFM) to image and track single oxygen nanobubbles in single cells. ONBs were proposed as promising contrast-generating imaging agents due to their strong light scattering generated from nonuniformity of refractive index at the interface. With this powerful platform, we have revealed the trajectories and quantities of ONBs in cells, and demonstrated the relation between the size and diffusion coefficient. We have also evaluated the presence of ONBs in the nucleus with respect to an increase in incubation time and have quantified the uptake in single cells in *ex vivo* tumor tissues. Our results demonstrate that HSDFM can be a versatile platform to detect and measure cellulosic nanoparticles at the single-cell level and to assess the dynamics and trajectories of this delivery system.

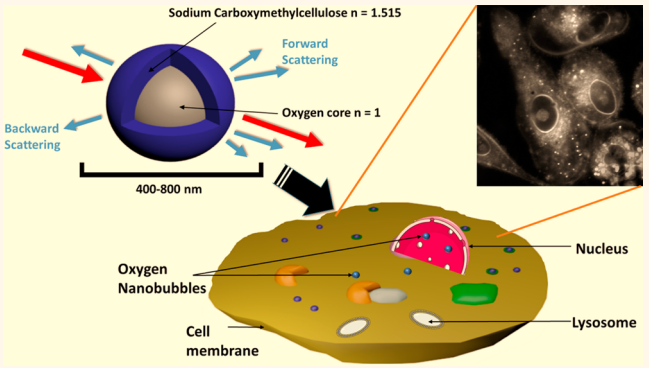

KEYWORDS: *oxygen nanobubbles, hyperspectral dark-field microscope, single cell analysis, tracking, quantification, diffusion*

Live-cell single particle imaging can characterize subcellular dynamics, measure motion properties within the cellular and extracellular environment, or even interactions of the particle with organelles, cell walls.[1,2] Single-particle tracking can enable the design of better drugs, understanding of cellular dynamics, and study of the transport phenomena of particles.[2,3] Hyperspectral imaging (HSI) is an approach that allows for a high-resolution spectrum to be acquired at each pixel in an image.[4−7] From the collected spectral signatures, the spatial distribution of the optically active probes can be accurately obtained.[6,7] Dark-field microscopy can achieve a high signal-to-noise ratio (SNR) by excluding the unscattered incident beam to generate a clear background, which enhances the contrast when imaging unstained samples.[6] Combining the dark-field illumination with an HSI module, a platform was developed for the identification of the location and composition of nanomaterials in biological specimens with better quantitative accuracy. This is possible, since spectral information on each dark-field imaging pixel can be obtained with our technique (see Supporting Information).[6,7] In comparison with fluorescence microscopy, the HSDFM approach suffers minimally from autofluorescence, photobleaching, and phototoxicity.[8]

In this work, a fast and robust optical spectral imaging approach is demonstrated to quantitatively image and dynamically detect oxygen nanobubbles (ONBs) using HSDFM. ONBs are shown to have a significant effect in halting tumor progression and in altering the cellular dynamics and hypoxia-adaptive processes of the tumor cell. Nanobubbles are an ideal imaging agent in HSDFM due to their intense scattering signal. Combining nanobubbles with HSDFM will provide us with a tremendous opportunity to understand and image dynamic events of nanoprobes and biomolecules, at the single-cell level. Our method was successfully applied to characterize nanobubbles of different sizes and incubation times, within the cellular microenvironment, cytoplasm, as well as the nucleus. Using the established method, quantification of nanobubble distribution and diffusion coefficient within the cell was performed, both, *in vitro* in live cells, as well as *ex vivo* in mouse tumor tissues. These results evidently demonstrate our strategy for single nanobubble tracking in biomolecule detection and drug delivery, which is not easily accessible by other methods.

Received: November 6, 2016
Accepted: March 7, 2017
Published: March 7, 2017

DOI: 10.1021/acsnano.6b07478
ACS Nano XXXX, XXX, XXX−XXX

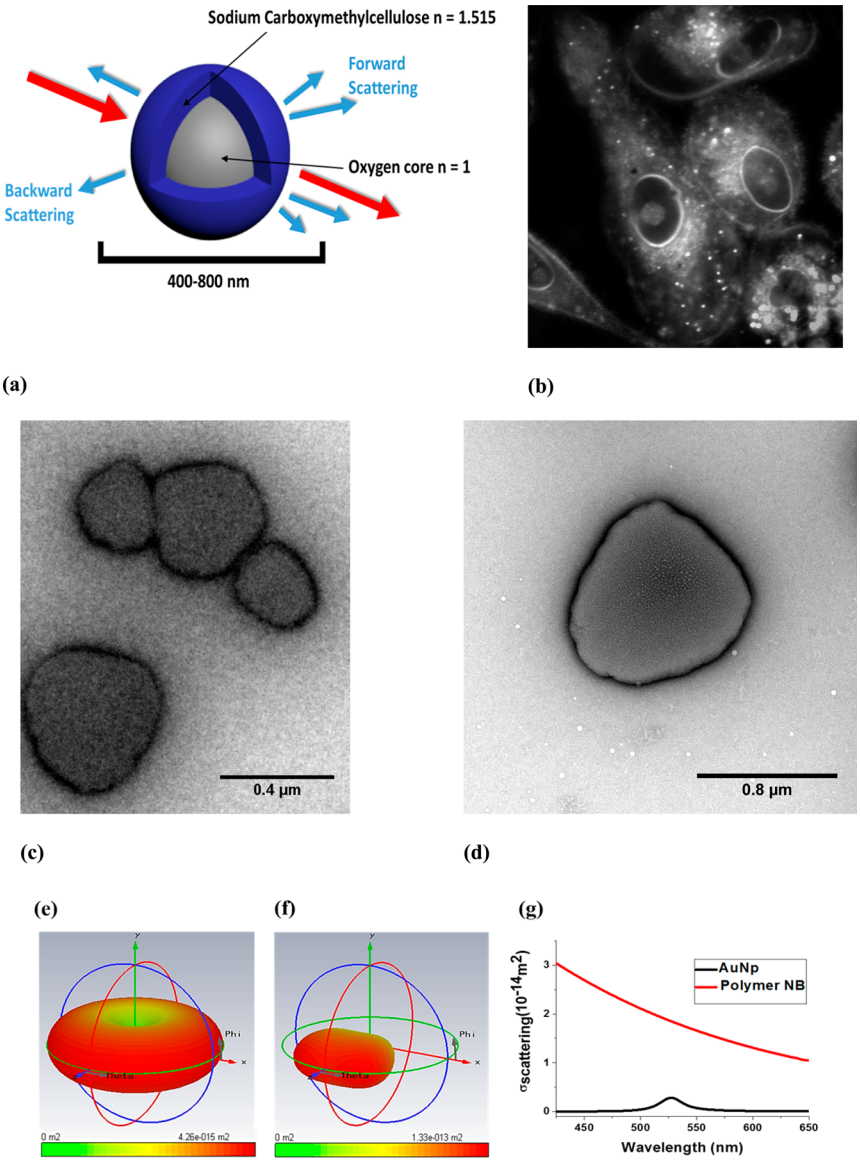

Figure 1. Illustration of quantitative detection of ONBs in cells with high signal-to-noise ratio and simulation results of far-field scattering. (a) Schematic illustrating the principle of dark field imaging using ONBs for optical contrast enhancement. Refractive index of different components is provided. (b) Dark-field optical image of 400 nm ONBs in PC3 cells. Transmission electron microscopy images showing 400 nm (c) and 800 nm (d) ONBs. (e) Angular scattering pattern of 40 nm AuNp in PBS. (f) Angular scattering pattern of 400 nm nanobubble in PBS. (g) Far-field scattering cross section of AuNp and nanobubble with different wavelengths. A plane wave incident source with linear polarization in the range of 330 to 660 THz was used in calculations.

RESULTS AND DISCUSSION

Optical Scattering from Nanobubbles. The synthesized ONBs consist of a gaseous molecular oxygen core surrounded by a cellulosic polymer shell (Figure 1a). This core–shell structure of the nanobubble causes nonuniformity of refractive index that is expected to force light to deviate from its linear trajectory to generate light scattering. The intensity and angular distribution of light scattering has a strong relation with the localized nonuniformities.[9] For scattering imaging, it is necessary to design nanomaterials with large nonuniformities in the refractive index range to obtain a high scattering signal from the probes to ensure a high signal-to-noise ratio. As depicted in Figure 1a,b, the refractive index of gas filled in an ONB is 1.0, while the refractive index of shell made of sodium carboxymethylcellulose is 1.515, and that of background medium is 1.3345 (phosphate buffered saline). ONB with a large difference in refractive index between the shell and the core was designed for this study to enable quantitative detection and tracking with single particle resolution. Two different sizes of nanobubbles, i.e., 400 and 800 nm, were synthesized using factorial design of experiments (Supporting Information Table S1) and optimized using response surface design (Supporting Information Section 4). Figure 1c,d shows transmission electron microscopy (TEM) images of ONBs with a size of 400 and 800 nm, respectively. The nanobubble shell was approximately 20 nm in thickness whereas the gaseous core was approximately 350 nm in diameter. We found that the nanobubbles of both sizes were monodisperse (Z average of 325.8 d-nm and 787.8 d-nm for 400 and 800 nm nanobubbles, respectively) and the polydispersity index was 0.374 for 400 nm and 0.632 for the 800 nm nanobubbles, respectively (Figures S5, S6). No multimodal peaks were obtained in either 400 or

DOI: 10.1021/acsnano.6b07478
ACS Nano XXXX, XXX, XXX–XXX

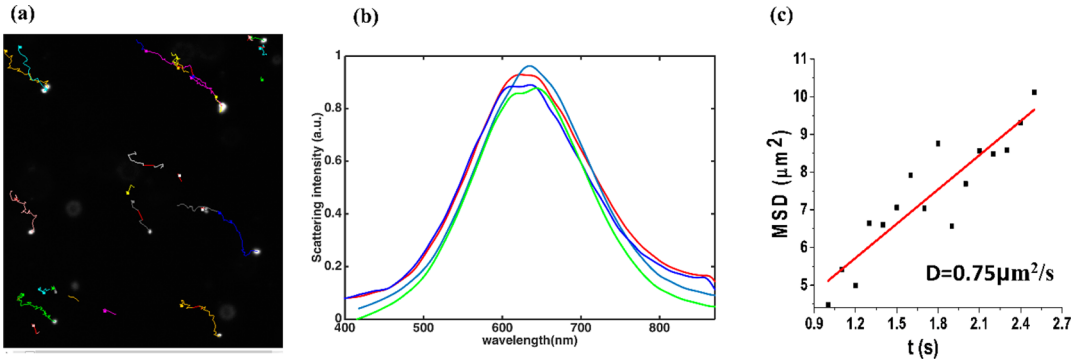

Figure 2. Illustration of single nanobubble (400 nm) tracking *in vitro*. (a) The trajectories of each ONBs are tracked by linking nanobubble positions in each time frame in the image stacks. (b) Normalized scattering spectras of 400 nm ONBs in PCR cells using HSDFI (n = 4). (c) Mean square displacement versus time. The diffusion coefficient of 400 nm ONBs in PBS is calculated based on linear fitting of mean square displacement with mean square displacement equation.

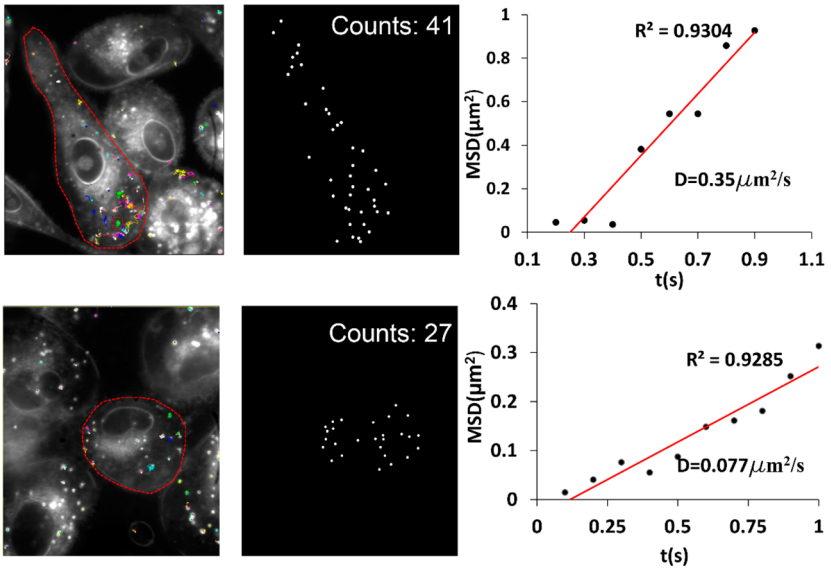

Figure 3. Precise quantification and tracking of ONBs with different diameters (400 nm (top) and 800 nm (bottom)). The left columns show the trajectories of each ONB in single PC3 cell. The middle column shows the quantification results of ONBs in cell after 2 h of incubation with ONBs, while the right column shows the diffusion coefficient of single ONB based on fitting of the mean square displacement.

800 nm nanobubbles and the cumulants fit error was less than 0.001 for both samples, indicating that the samples were monodisperse. The delivery of ONBs into the cell is expected to produce a large light scattering signal due to the large refractive index difference of ONB (Figure 1b) for molecular reporting. Further, theoretical calculations of far field angular scattering pattern and scattering cross section were also performed to illustrate the mechanics of ONB scattering. Furthermore, ONBs radiate light out in all directions in the XZ plane (Figure 1f), whereas gold nanoparticles (Figure 1e) radiate light in a localized angular range. The narrower scattering angle of ONBs helps concentrate the scattering intensity within a confined space. The directional scattering of ONBs will help increase the collected signal intensity by the microscope objective. Figure 1g shows that the scattering cross section of ONB is much larger than that of a gold nanoparticle.

Single Nanobubble Tracking and Quantification in Cancer Cell Lines. The number of ONBs and individual nanobubble tracking were determined using the scattering spectral signature with HSDFM. First, *in vitro* single ONB tracking was performed to evaluate the tracking efficiency. As illustrated in Figure 2, the trajectories of each ONB were obtained by linking ONB positions in the image stacks for each frame of time. Further details of the tracking process are described in the Supporting Information Section 2. The spectra obtained from the cellular organelles and nanobubbles were used to further distinguish the two materials. We found that the spectras of 400 nm nanobubbles are reproducible with minor differences in peak positions and spectral width (Figure 2b). The diffusion coefficient of ONB in PBS buffer was found to be 0.75 $\mu m^2/s$ (Figure 2c) derived using regression analysis based on trajectories (Supporting Information Section 2). This set of *in vitro* characterization of ONBs demonstrates the optical validity of our method for the detection of specific nanobubbles in cells and tissues.

Estimation of the diffusion coefficient is very important for studying the dynamics of ONBs as a drug carrier in cells and to understand the mechanism of drug delivery. The size of ONB is a crucial factor in determining its interaction with cells and distribution in the biological system. The ability of nanoparticles to extravasate from the vasculature and also their clearance from circulation depends on their size.[10−12] This is an

DOI: 10.1021/acsnano.6b07478
ACS Nano XXXX, XXX, XXX−XXX

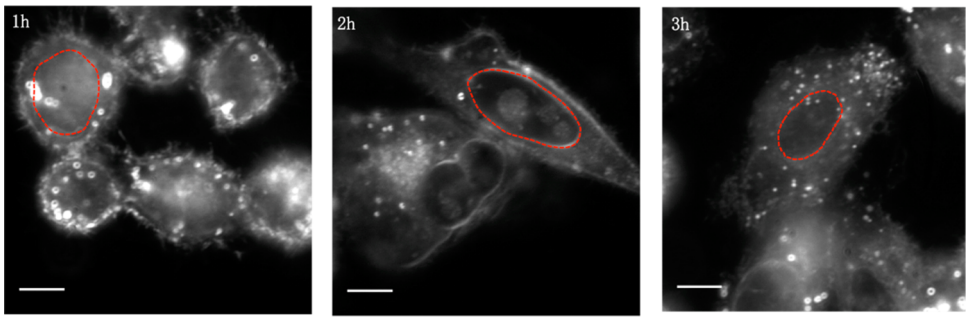

Figure 4. Dark field optical images of PC3 cells incubated with 400 nm ONBs with different incubation time. Nucleus highlighted using red dotted line. ONB uptake into the nucleus increases over the time period evaluated (3 h). Scale bar = 5 μm.

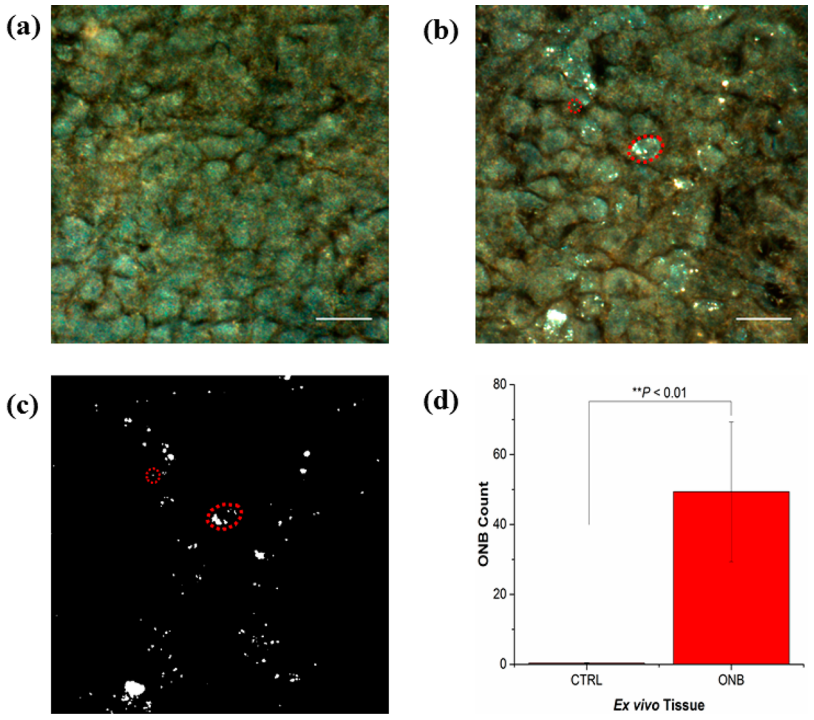

Figure 5. Quantitative detection of 400 nm ONBs in subcutaneously implanted Mb49 bladder cancer tissue in mice. (a) Representative dark-field optical image of MB49 mouse bladder cancer tissue treated with saline (control). (b) Representative dark-field optical images of Mb49 mouse bladder cancer tissue with ONBs. Single ONB used as reference was circled with red dotted lines, while cell was circled with ellipse red dotted line. (c) Representative gray scale image of ONBs with intensity threshold filter processing. (d) Number of ONBs in single cell in *ex vivo* tissues treated with saline (CTRL) or nanobubbles (ONB) (N = 9, P < 0.01).

important consideration for ONB drug carriers since longer circulating ONBs will have a higher chance of reaching their target,[13−15] resulting in improved treatment outcome. Our first set of experiment was thus performed to evaluate the number and diffusion coefficient of ONBs with different size in single cells. PC3 human prostate cancer cell lines were incubated with 400 and 800 nm ONBs for 2 h. Dark-field optical images sequences were obtained with 100 ms frame interval. Since cellular organelles were stationary compared to ONBs, the bubbles were located in the cells by tracking their movement in each frame, as shown in Figure 3 (see Supporting Information Video). Cellular uptake efficiency was calculated using NanoTrackJ plugin[16] in ImageJ software. The number of nanobubbles per cell were counted using the plugin with the mean filter and tolerance levels adjusted to be the same for all the images. We found that the cellular uptake efficiency for 400 nm ONBs was ∼88% higher than the 800 nm nanobubbles (P < 0.01). Further, the intranuclear uptake efficiency was ∼56% higher for the 400 nm nanobubbles compared to the 800 nm nanobubbles (P < 0.01) possibly due to enhanced uptake of the smaller sized nanoparticles via endocytosis[17] compared to fluid-phase pericytosis of larger sized nanoparticles.[18] Literature supports our findings in that the efficiency of nanoparticle uptake is indirectly proportional to the size of the nanoparticle.[19,20]

Further, we calculated the diffusion coefficients of ONBs based on trajectory tracking, linear fitting of mean square displacement, and 2D mean square displacement equation. The linear model was found to be an appropriate fit for the data obtained (R^2 > 92%). It was observed that as the size of ONB increases, the diffusion coefficient decreases (Figure 3). Diffusion coefficient can be expressed as,

$$D = (1/f)*k*T \quad (1)$$

where f is the frictional coefficient, k is Boltzmann constant, and T is the absolute temperature. Frictional coefficient has a direct

DOI: 10.1021/acsnano.6b07478
ACS Nano XXXX, XXX, XXX−XXX

relation with viscosity and diameter of nanobubble.[21] When the size of ONB increases, the frictional coefficient increases due to larger surface area of the ONB, and this results in an increase in the diffusion coefficient. These results support the identification and tracking capability of our optical scattering method.

Efficient delivery of drug loaded nanoparticles to the nucleus of tumor cells is critical for enhancing the efficacy of targeted drug delivery.[22,23] The ONB is expected to significantly enhance drug delivery to the nucleus of the cells due to its size. To study the cellular and nuclear uptake efficiency of ONBs, we performed *in vitro* experiments using prostate cancer cells (PC3) with 400 nm ONBs and different incubation time. As shown in Figure 4, no ONBs were observed inside the cells after 1 h of incubation. As the incubation time increased to 2 h, some ONBs were observed in the cytoplasm of the cells due to endocytosis. However, no ONBs were observed in the nucleus after 2 h. Further, ONBs gradually penetrated the nuclear membrane, and entered the nucleus as incubation time increased to 3 h (see Supporting InformationVideo). Our results indicate that the light scattering approach using dark field microscopy to characterize the biophysical properties of ONBs s is a promising approach for use as both, an optical imaging agent as well as a drug delivery enhancer.

Single Nanobubble Quantification in Bladder Tumor Tissue. We further studied the potential of ONBs and HSDFM for *ex vivo* quantitative analysis of biodistribution in different tissues. *In vitro*, the diffusion of ONBs within the cell and its environment can be utilized to distinguish them from static intracellular organelles. However, for *ex vivo* analysis of ONBs in paraffin embedded or cryosectioned tissue samples, hyperspectral information analysis was used to distinguish ONBs from static cellular organelles instead of movement analysis since the motion of ONBs is hindered in the paraffin embedded slides. According to Mie scattering,[24] some intracellular organelles with size on the same order of the wavelength of incident light have large scattering, and the scattering color is white due to the broad spectrum. The scattering color of ONBs was found to be white, making it difficult to differentiate ONBs from intracellular organelles with dark-field optical images (Figure S2). Nevertheless, the spectrum information was utilized to distinguish ONBs from the intracellular organelles. Different sized ONBs have unique scattering spectra; the spectrum "red shifts" as the nanoparticle size increases.[25,26] As illustrated in Figure S2, experiments in this study were performed with 400 nm ONBs, which have a different spectrum than the cell organelles in the cytoplasm.

To validate our technique *ex vivo*, MB49 mouse bladder cancer cell line was implanted subcutaneously into mice and treated with ONBs (see Materials and Methods Section). The tumors were excised in formalin, embedded in paraffin, and sectioned at a thickness of 10 μm. Negative control experiments were also performed to prove the specificity of the ONB. From Figure 5a,b, it is evident that ONBs have a strong scattering signal, and results in optical dark-field images with high signal-to-noise ratio. Using intensity threshold filter, gray scale images of ONBs were obtained (Figure 5c). After excluding the background noise with intensity threshold, improved quantification information can be obtained. Further, we quantified the number of nanobubbles in *ex vivo* mouse tumor tissue treated with either saline (CTRL) or ONB (Figure 5d) using MTrackJ[16] plugin in ImageJ. We found that ONBs could be accurately detected using our technique in *ex vivo* tumor tissues.

DISCUSSION

Our experiments point to the key advantages of high-resolution imaging and tracking of ONBs using HSDFM. The major advantage of our technique is the strong signal from single ONB due to the large light scattering cross-section, which makes the quantification and tracking of ONB with high SNR at the single-cell level possible. As evident from Figure S4, the SNR of ONB is much higher than that of gold nanoparticle, which has been extensively utilized as imaging nanoprobes due to their strong localized surface plasmon resonance scattering cross-section. Owing to the dipole resonance from the interaction with incident photons, the large scattering cross-section of plasmonic NPs can generate a ten- to million-fold stronger signal than conventional fluorophores. Nevertheless, compared to gold nanoparticles with size of 40 nm, ONBs have larger light scattering, as demonstrated in our *in vitro* results (Figure S4).

Our work demonstrates the feasibility of HSDFM for tracking and visualization of ONBs in single cells based on light scattering. By fabricating the ONBs to have a high refractive index difference between core and shell, the scattering cross section can be significantly enhanced, which constitutes the scientific base of our strategy. We applied this method to analyze the relation between the size of ONB and its diffusion characteristics, quantification of ONBs in single cell, and uptake of ONB by cells with time and to assess its distribution in the cell cytoplasm and nucleus. The methods developed can be utilized to count ONBs in *ex vivo* bladder tumor tissue. Our technique is broad and can be applied to a range of systems to track drug-loaded ONB's in tissue cultures, assess its endocytosis mechanisms and distribution *ex vivo* in various tissues. Further, the dynamics and kinetics of cellular uptake and the role of the cytoskeleton, *in vitro* and *ex vivo* can be effectively studied using the developed tools. Finally, fundamental molecular mechanisms in living cells can also be revealed by utilizing the power of HSDFM and ONBs.

CONCLUSION

In conclusion, our results demonstrate the capability of the proposed light scattering method with hyperspectral dark-field imaging microscope for quantitative detection and tracking of ONB in single living cell and identification in tissues. Taking advantage of the ONB's strong light scattering signal due to its noncontinuous refractive index, we can effectively identify the relationships between ONB and their size distribution, diffusion coefficients within a single cell, and biodistribution and pharmacokinetic distribution in *ex vivo* tissue. Our technique can effectively circumvent the common limits that conventional imaging techniques suffer from, to provide a better signal-to-noise ratio for high-resolution biological imaging with a simple hyperspectral dark-field imaging microscope and image analysis. Our approach demonstrates single nanobubble tracking in the field of nanoparticle localization and targeting in single cells. The proposed contrast agent can be expanded for *ex vivo* tissue histology and pharmacokinetic/pharmacodynamics studies, in clinical diagnosis and targeted therapy.

MATERIALS AND METHODS

Preparation of Nanobubbles. Oxygen nanobubbles were synthesized by cross-linking of sodium carboxymethylcellulose with oxygen entrapment. Size distribution of the nanobubbles was optimized using a fractional factorial design of experiments to screen for significant parameters followed by a full factorial design (Table S1)

DOI: 10.1021/acsnano.6b07478
ACS Nano XXXX, XXX, XXX−XXX

to obtain nanobubbles in the size range 400−800 nm (see Supporting Information). Briefly, sodium carboxymethylcellulose (Aqualon 7HF PH, Ashland Inc., Calumet City, IL) was dissolved in nanopure water to form a 0.1% (w/v) gel and homogenized and saturated with oxygen gas (UHP grade). The oxygen inlet was connected with an air nozzle (Nano Super Air Nozzle 1110SS, EXAIR Corporation) and a 20 nm membrane filter (Emflon II, Pall Corporation) to help generate ONBs. The carboxymethyl cellulose solution was sonicated simultaneously with a probe (Ultrasonic Power Corporation Cell Disrupter) and a bath sonicator (Branson 2210) for 30−120 s since ultrasonic energy helps sonic compression of oxygen microbubbles to produce oxygen nanobubbles in the solution.[27] Finally, 0.1−1% aluminum chloride ($AlCl_3$) cross-linking agent was added to form the encapsulation structure under continuous ultrasonication. Aluminum chloride is a trivalent cross-linker and helps decrease the drug release rate[28] compared to bivalent cross-linkers. Aluminum chloride also serves as a strong electrolyte and increases the electrostatic repulsive force to balance out the size reduction forces of the nanobubble, thus stabilizing the nanobubble.[29] The pH of the resulting nanobubble suspension was subsequently neutralized to a pH of 7 using 0.1−0.5% ammonium hydroxide (NH_4OH) solution added dropwise. Finally, the significant parameters were optimized using the prediction profile of the data in JMP (SAS Institute Inc.).

PC3 Cell Culture and Nanobubbles Uptake. Human epithelial prostate cancer cell line, PC3 (ATCC CRL-1435), was used for *in vitro* experiments because of its widely studied biochemical profile in response to several chemotherapeutic agents across various experimental conditions. Cells were cultured in RPMI-1640 media (Gibco, Life Technologies) supplemented with 10% Fetal Bovine Serum (Atlanta Biologicals, Flowery Branch, GA) and 1% Penicillin (10 000 IU/mL) -Streptomycin (10 000 μg/mL) (Mediatech Inc., Manassas, VA). The cells were routinely cultured at 37 °C in a humidified atmosphere with 5% CO_2. Cells were tested for mycoplasma contamination using Hoechst 33258 fluorescent indirect staining[30] before initiating the experiments. Briefly, cells were fixed using 4% paraformaldehyde (PFA) solution and stained with Hoechst 33258 fluorescent dye. Images were obtained using the confocal microscope. No small specks were observed surrounding the cells thus confirming the absence of mycoplasma. The cells were incubated with ONBs (0.1 mg/mL) in a 12-well plate and imaged at different time points.

***Ex Vivo* Quantification of Nanobubbles in MB49 Mouse Bladder Cancer Tissue.** Animals were cared for under the supervision of the Purdue Animal Care and Use Committee (PACUC). Briefly, MB49 cells (5×10^5 cells/mouse) in the media were subcutaneously injected in female 6−8 weeks old C57Bl/6 mice since C57Bl/6 mice are a syngenic model for MB49 cell line and are immunocompetent. Number of replicates required for the study was calculated using the power law analysis for *in vitro* and preliminary *in vivo* data using a desired power of test of 90% and alpha of 5%. After 3 weeks when tumors develop hypoxia and reach an approximate size of 1000 mm^3, the mice were randomly divided into two groups of five and six. Tumor-bearing mice were treated by intravenous injections of ONBs (100 μg/mL, 100 μL, $n = 6$) or saline (100 μL, $n = 5$). After dosing, the mice were monitored for weight and implanted tumor size daily. Four days following bolus injections, mice were euthanized via cardiac puncture and the blood and organs were harvested. Harvested tissues and tumors were fixed in formalin-free IHC Zinc Fixative (BD Pharmingen), embedded in paraffin, and sectioned into 5 μm slices. Histology slides were prepared at the Purdue Histology and Phenotyping Laboratory (PHPL).

Hyperspectral Image Acquisition. HSDFM generates a 3D data set of spatial and spectral information at each pixel. Hyperspectral data can be obtained by stacking the 1D spectra image along the x-coordinate (slit) by scanning the sample-stage along the *y*-axis. First, dark-field images were obtained to determine the region of interest (ROI). The detector was uniformly illuminated to acquire a flatfield file to exclude small nonuniformities in gain on a pixel-by-pixel basis for correction. Then premeasurement was performed with 1D spectral imaging to set the light illumination level, which was optimized to have a maximum signal without saturation, critical for signal normalization. With these preset parameters, 1D spectral image was obtained by projecting the image onto a 10-μm slit, followed by dispersing the slit image with 300 g/mm grating to obtain a high spectral resolution of 0.5 nm. With a line-scanning stage of 40 nm step size, the spectral information on the 2D spatial dimension was collected over the wavelength range from 400 to 950 nm. Stabilized mounts guarantee the accurate position information for reconstruction of the images. Hyperspectral images spanning the entire ROI at each wavelength channel can then be constructed from the collected 1D spectral images with a data analysis algorithm.

Simulation of Scattering. 3D finite-difference time-domain (FDTD) numerical simulation analysis was used to calculate the far-field angular scattering patterns of ONBs at one specific wavelength (Figure 2), and the scattering cross sections of GNPs and ONBs within different incident wavelength (Figure 2). To match actual experiment, our model was designed as a 40 nm GNP or a nanobubble sphere (RI = 1.515 for shell, RI = 1.0 for core) immersed in infinite background material with the RI value of 1.33. Drude model[31] was used to describe the dispersion of gold atoms. A plane wave incident source with linear polarization was applied to calculate the far field angular scattering pattern and scattering cross section. For calculating the far-field angular scattering pattern of ONBs, the frequency was set to 545 THz, the local surface plasmon resonance (LSPR) wavelength of a 40 nm GNP. The scattering cross sections of GNPs and ONBs of size 400 nm were simulated from 330 to 660 THz, corresponding to our experimental illumination source. A fast perfect boundary approximation mesh was used to eliminate staircase error at the interface for accurate simulation. A far-field monitor was used to obtain the 3D radar cross section which subsequently determined the far-field angular scattering pattern. The broadband scattering response was extracted by using a broadband far-field monitor in combination with the broadband far-field template, which allowed the direct extraction of the extinction cross section and scattering cross section. Since the simulation was calculated based on frequency, a "Mix 1D" result template was then used to convert the *x*-axis from frequency to wavelength domain in the plot.

ASSOCIATED CONTENT

Supporting Information

The Supporting Information is available free of charge on the ACS Publications website at DOI: 10.1021/acsnano.6b07478.

HSDFM instrumentation and image processing; algorithm for quantification and diffusion coefficient; algorithm for quantification of ONB in tissue; nanobubble synthesis and optimization; dark-field optical images of nanobubble of different size and PC3 cell without nanobubble; spectra of nanobubbles and cell organelle in PC3 cell were extracted from hyperspectral data; simulated far-field scattering with CST studio suite 2014 software; far-field scattering cross section of nanobubble dimer with different gap distance; electronic field intensity distribution with difference gap distance at 545 THz; plane wave incident source with linear polarization in the range of 330 to 660 THz; dark-field optical images of 40 nm AuNp and 400 nm oxygen nanobubble *in vitro*; prediction profile for the optimization of nanobubble size; DLS size distribution for 400 nm and 800 nm nanobubbles; therapeutic potential of ONB for PC3 cell line with 24 h incubation time; therapeutic potential of ONB for PC3 cell line with 48 h incubation time; 400 nm nanobubble quantification using dark-field imaging for *in vitro* assays; and 800 nm nanobubble quantification using dark-field imaging for *in vitro* assays (PDF)

Darkfield microscopy videos showing intracellular and intranuclear localization of oxygen nanobubbles (ONB)

DOI: 10.1021/acsnano.6b07478
ACS Nano XXXX, XXX, XXX−XXX

in vitro, ONB paths tracked using MtrackJ plugin in ImageJ (AVI)

AUTHOR INFORMATION

Corresponding Author

*E-mail: josephi@purdue.edu.

ORCID

Joseph Irudayaraj: 0000-0002-0630-1520

Author Contributions

§P.B. and X.W. contributed equally.

Notes

The authors declare the following competing financial interest(s): P.B. and J.I. declare potential financial interest in the future development and commercialization of similar nanomaterials. Office of Technology and Commercialization (OTC) of Purdue Research Foundation (PRF) has filed non-provisional patent USSN: 14/873,208 for the technology.

ACKNOWLEDGMENTS

The authors acknowledge funding from the W.M. Keck Foundation and the IDDA grant from the Indiana CTSI. Support from the Purdue University Center for Cancer Research, NIH grant P30 CA023168 is appreciated.

REFERENCES

(1) Jaqaman, K.; Loerke, D.; Mettlen, M.; Kuwata, H.; Grinstein, S.; Schmid, S. L.; Danuser, G. Robust Single-Particle Tracking in Live-Cell Time-Lapse Sequences. *Nat. Methods* **2008**, *5*, 695−702.

(2) Zhu, L.; Wu, W.; Zhu, M.-Q.; Han, J. J.; Hurst, J. K.; Li, A. D. Reversibly Photoswitchable Dual-Color Fluorescent Nanoparticles as New Tools for Live-Cell Imaging. *J. Am. Chem. Soc.* **2007**, *129*, 3524−3526.

(3) Li, Y.-P.; Pei, Y.-Y.; Zhang, X.-Y.; Gu, Z.-H.; Zhou, Z.-H.; Yuan, W.-F.; Zhou, J.-J.; Zhu, J.-H.; Gao, X.-J. Pegylated PLGA Nanoparticles as Protein Carriers: Synthesis, Preparation and Biodistribution in Rats. *J. Controlled Release* **2001**, *71*, 203−211.

(4) Lee, K.; Drachev, V. P.; Irudayaraj, J. DNA− Gold Nanoparticle Reversible Networks Grown on Cell Surface Marker Sites: Application in Diagnostics. *ACS Nano* **2011**, *5*, 2109−2117.

(5) Lee, K.; Cui, Y.; Lee, L. P.; Irudayaraj, J. Quantitative Imaging of Single mRNA Splice Variants in Living Cells. *Nat. Nanotechnol.* **2014**, *9*, 474.

(6) Cui, Y.; Wang, X.; Ren, W.; Liu, J.; Irudayaraj, J. Optical Clearing Delivers Ultrasensitive Hyperspectral Dark-Field Imaging for Single-Cell Evaluation. *ACS Nano* **2016**, *10*, 3132−3143.

(7) Wang, X.; Cui, Y.; Irudayaraj, J. Single-Cell Quantification of Cytosine Modifications by Hyperspectral Dark-Field Imaging. *ACS Nano* **2015**, *9*, 11924−11932.

(8) Cui, Y.; Irudayaraj, J. Inside Single Cells: Quantitative Analysis with Advanced Optics and Nanomaterials. *Wiley Interdiscip. Rev.: Nanomed. Nanobiotechnol.* **2015**, *7*, 387−407.

(9) Hulst, H. C.; van de Hulst, H. C. *Light Scattering by Small Particles*; Courier Corporation, 1957.

(10) Maeda, H.; Wu, J.; Sawa, T.; Matsumura, Y.; Hori, K. Tumor Vascular Permeability and the EPR Effect in Macromolecular Therapeutics: A Review. *J. Controlled Release* **2000**, *65*, 271−284.

(11) Greish, K. Enhanced Permeability and Retention of Macromolecular Drugs in Solid Tumors: A Royal Gate for Targeted Anticancer Nanomedicines. *J. Drug Targeting* **2007**, *15*, 457−464.

(12) Prabhakar, U.; Maeda, H.; Jain, R. K.; Sevick-Muraca, E. M.; Zamboni, W.; Farokhzad, O. C.; Barry, S. T.; Gabizon, A.; Grodzinski, P.; Blakey, D. C. Challenges and Key Considerations of the Enhanced Permeability and Retention Effect for Nanomedicine Drug Delivery in Oncology. *Cancer Res.* **2013**, *73*, 2412−2417.

(13) Bae, Y. H.; Park, K. Targeted Drug Delivery to Tumors: Myths, Reality and Possibility. *J. Controlled Release* **2011**, *153*, 198.

(14) Park, K. Facing the Truth About Nanotechnology in Drug Delivery. *ACS Nano* **2013**, *7*, 7442−7447.

(15) Yoo, J.-W.; Chambers, E.; Mitragotri, S. Factors That Control the Circulation Time of Nanoparticles in Blood: Challenges, Solutions and Future Prospects. *Curr. Pharm. Des.* **2010**, *16*, 2298−2307.

(16) Wagner, T.; Lipinski, H.-G.; Wiemann, M. Dark Field Nanoparticle Tracking Analysis for Size Characterization of Plasmonic and Non-Plasmonic Particles. *J. Nanopart. Res.* **2014**, *16*, 2419.

(17) Chithrani, B. D.; Chan, W. C. Elucidating the Mechanism of Cellular Uptake and Removal of Protein-Coated Gold Nanoparticles of Different Sizes and Shapes. *Nano Lett.* **2007**, *7*, 1542−1550.

(18) Boudad, H.; Legrand, P.; Appel, M.; Coconnier, M.-H.; Ponchel, G. Formulation and Cytotoxicity of Combined Cyclodextrin Poly (Alkylcyanoacrylate) Nanoparticles on Caco-2 Cells Monolayers Intended for Oral Administration of Saquinavir. *STP Pharma Sci.* **2001**, *11*, 369−375.

(19) Win, K. Y.; Feng, S.-S. Effects of Particle Size and Surface Coating on Cellular Uptake of Polymeric Nanoparticles for Oral Delivery of Anticancer Drugs. *Biomaterials* **2005**, *26*, 2713−2722.

(20) Desai, M. P.; Labhasetwar, V.; Walter, E.; Levy, R. J.; Amidon, G. L. The Mechanism of Uptake of Biodegradable Microparticles in Caco-2 Cells Is Size Dependent. *Pharm. Res.* **1997**, *14*, 1568−1573.

(21) Dill, K.; Bromberg, S. *Molecular Driving Forces: Statistical Thermodynamics in Biology, Chemistry, Physics, and Nanoscience*; Garland Science, 2010.

(22) Torchilin, V. P. Recent Approaches to Intracellular Delivery of Drugs and DNA and Organelle Targeting. *Annu. Rev. Biomed. Eng.* **2006**, *8*, 343−375.

(23) Farokhzad, O. C.; Langer, R. Impact of Nanotechnology on Drug Delivery. *ACS Nano* **2009**, *3*, 16−20.

(24) Mundy, W.; Roux, J.; Smith, A. Mie Scattering by Spheres in an Absorbing Medium. *J. Opt. Soc. Am.* **1974**, *64*, 1593−1597.

(25) Fleger, Y.; Rosenbluh, M. Surface Plasmons and Surface Enhanced Raman Spectra of Aggregated and Alloyed Gold-Silver Nanoparticles. *Res. Lett. Opt.* **2009**, *2009*, 1−5.

(26) Thomas, S.; Nair, S. K.; Jamal, E. M. A.; Al-Harthi, S.; Varma, M. R.; Anantharaman, M. Size-Dependent Surface Plasmon Resonance in Silver Silica Nanocomposites. *Nanotechnology* **2008**, *19*, 075710.

(27) Cho, S.-H.; Kim, J.-Y.; Chun, J.-H.; Kim, J.-D. Ultrasonic Formation of Nanobubbles and Their Zeta-Potentials in Aqueous Electrolyte and Surfactant Solutions. *Colloids Surf., A* **2005**, *269*, 28−34.

(28) Nokhodchi, A.; Tailor, A. In Situ Cross-Linking of Sodium Alginate with Calcium and Aluminum Ions to Sustain the Release of Theophylline from Polymeric Matrices. *Farmaco* **2004**, *59*, 999−1004.

(29) Chiba, K.; Takahashi, M. Oxygen Nanobubble Water and Method of Producing the Same. US Patent US20070286795 A1, 2007.

(30) Young, L.; Sung, J.; Stacey, G.; Masters, J. R. Detection of Mycoplasma in Cell Cultures. *Nat. Protoc.* **2010**, *5*, 929−934.

(31) Bade, W. Drude-Model Calculation of Dispersion Forces. I. General Theory. *J. Chem. Phys.* **1957**, *27*, 1280−1284.

DOI: 10.1021/acsnano.6b07478
ACS Nano XXXX, XXX, XXX−XXX